This is the preprint version of the following article:

Van Helden T, Mervič K, Nemet I, T. van Elteren J, Vanhaecke F, Rončević S, Šala M, Van Acker T. Evaluation of two-phase sample transport upon ablation of gelatin as a proxy for soft biological matrices using nanosecond laser ablation – inductively coupled plasma – mass spectrometry. *Analytica Chimica Acta*. 2024; (1287): 1—11.

which has been published in final form at:

https://doi.org/10.1016/j.aca.2023.342089

Evaluation of two-phase sample transport upon ablation of gelatin as a proxy for soft biological matrices using nanosecond laser ablation – inductively coupled plasma – mass spectrometry

Tom Van Helden [a], Kristina Mervič [b,c], Ivan Nemet [d], Johannes T. van Elteren [b], Frank Vanhaecke [a], Sanda Rončević [d], Martin Šala [b], Thibaut Van Acker * [a]

[a] Department of Chemistry, Atomic & Mass Spectrometry – A&MS Research Group, Ghent University, Campus Sterre, Krijgslaan 281-S12, BE-9000, Ghent, Belgium

[b] National Institute of Chemistry, Hajdrihova 19, SI-1000 Ljubljana, Slovenia

[c] Jožef Stefan International Postgraduate School, Jamova Cesta 39, SI-1000, Ljubljana, Slovenia

[d] Department of Chemistry, Faculty of Science, University of Zagreb, Horvatovac 102a, 10000 Zagreb, Croatia

* Corresponding author, phone number: +3292644851, e-mail: Thibaut.VanAcker@UGent.be

Abstract

Background: Recent papers on LA-ICP-MS have reported that certain elements are transported in particulate form, others in gaseous form and still others in a combination of both upon ablation of C-based materials. These two phases display different transport behaviour characteristics, potentially causing smearing in elemental maps, and could be processed differently in the ICP which raises concerns as to accuracy of quantification and emphasizes the need for matrix-matching of external standards. This work aims at a better understanding of two-phase sample transport by evaluating the peak profile changes observed upon varying parameters such as laser energy density and wavelength.

Results: It is demonstrated that upon ablation of gelatin, elements are transported predominantly in particulate phase but already at low laser energy density, a significant fraction of some elements is transported in the gaseous phase, which is even more expressed at higher energy density. This behaviour is element-specific and was demonstrated as the ratio of signal intensity for the analyte element transported in gas phase to the total signal intensity was 0% for ^{23}Na, 43% for ^{66}Zn and as high as 95% for ^{13}C using a 193 nm laser. The results also suggest an effect of the laser wavelength, as all elements show either the same or higher amount of gas phase formation upon ablating with 213 nm versus 193 nm. It was even established that elements that fully occur in particulate form upon ablation using 193 nm laser radiation are partly converted into gaseous phase when using 213 nm.

Significance: This work provides a thorough investigation of the underexposed phenomenon of two-phase sample transport upon ablation of biological samples upon via LA-ICP-MS. It is

shown that for some elements a fraction of the ablated material is converted and transported in the gas phase, which leads to significant smearing effects. As such, it is important to evaluate element-specific peak profiles on beforehand and, if necessary, adapt instrument settings and slow down data acquisition conditions.

Keywords

Laser ablation (LA), inductively coupled plasma-mass spectrometry (ICP-MS), gelatin, two-phase sample transport

1. Introduction

Since the first application of laser ablation – inductively coupled plasma-mass spectrometry (LA-ICP-MS) for direct solid sample elemental analysis using a microsecond 694 nm ruby laser by Gray et al. in 1985 [1], LA-ICP-MS has been mainly applied to the analysis of either hard-to-dissolve materials such as rocks and minerals in the research fields of the earth sciences, or precious materials for which only limited sample consumption was allowed, such as forensic evidence, archaeological artefacts and gemstones [2-8]. One of the major drawbacks of the technique established during the early years was that the recorded signals and signal ratios were not always representative for the stoichiometry of the sample. This phenomenon was called elemental fractionation with the latter being considered the umbrella term for the non-stoichiometric effects occurring during all related processes, e.g., laser ablation, aerosol transport, vaporization, atomization and ionization in the ICP, and leading to a mismatch between the measured relative signal intensities and the actual sample composition [9]. Since laser-matter interactions were believed to be the main source of elemental fractionation, fundamental studies were focused on evaluating different types of lasers in terms of wavelength and pulse duration to reduce elemental fractionation and improve the overall analytical performance using glass reference materials such as the NIST SRM 61X series [9-12]. This resulted in a clear shift towards the use of deep-UV lasers, e.g., fourth (266 nm) and fifth (213 nm) harmonic Nd:YAG lasers and ArF* excimer-based lasers (193 nm), which reduced these effects significantly. It was also demonstrated that incomplete vaporization of glass aerosol particles with a diameter larger than 150 nm in the ICP represented the main source of elemental fractionation [13-15]. In addition, the absorption characteristics of the sample material, determined by the bulk composition, influence the aerosol particle size distribution at a specific wavelength [16]. In general, for non-metallic materials, the higher the absorption, the lower the penetration depth of the photon beam and the lower the ablation yield (ablated mass per laser pulse), but the smaller the average particle size which is beneficial for the efficiency of aerosol transport and ICP-related processes [9]. Upon interaction of the laser pulse with the sample surface, particles and/or vapor are being formed [17]. Via condensation of the supersaturated vapor, particles are formed with a typical size of

tens of nanometers as, due to the fast cooling rate, larger particles cannot be formed by condensation processes. Agglomeration due to collisions between particles can subsequently lead to larger-sized particles [15, 18]. Particle-size dependent fractionation has been demonstrated for ablation of brass samples with nanosecond laser radiation, since particles > 100 nm consisted primarily of Cu, while smaller particles and vapor were enriched in Zn as a result of heating and vaporization of ejected particles in the laser-induced plasma. Metal vapor and small particles were found to be completely atomized and ionized within the ICP, while the larger Cu-enriched particles were not fully vaporized leading to lower Cu signal intensities [19, 20].

Most of these fundamental studies were focused on hard-to-dissolve materials, such as glass, metals, minerals and rocks, but also significant fundamental work was performed on carbon (C)-based materials such as polymers and biological tissues [21]. Especially for the latter sample types, the lack of readily available certified reference materials and calibration standards complicates quantitative analysis and therefore, many labs are relying on in-house external calibration standards often in combination with C as an internal standard to correct for differences in ablation yield, matrix effects and signal drift [22-28]. Significant concerns were raised by the community about the applicability of C as an internal standard because of its high first ionization energy (11.3 eV), potentially leading to substantial signal intensity variations upon slight changes in the ICP conditions [29]. Pioneering work of Todolí and Mermet [30] also demonstrated two-phase sample transport upon ablation of various types of polymers. They reported up to 80% of C being transported in the gaseous phase rather than in particulate form, as a result of which C cannot be considered the ideal internal standard. Frick et al. [28] confirmed these findings and proved that the degree of gaseous phase formation was strongly matrix-dependent (affected by the oxygen/carbon ratio) and reported that also sulphur was partly transported in the a gaseous phase. In a later work, Frick *et al*. have also reported on the formation of a gaseous phase for iodine, as observed upon passing the laser-generated aerosol through a gas exchange device [31].

This formation of a gaseous phase cannot only lead to problems in the context of internal standardisation, but also when a gaseous phase is formed for analyte elements. While performing elemental mapping for revealing the spatial distribution of Hg, an element notoriously prone to evaporation, Debeljak *et al.* [32] reported long, tailing signals caused by memory effects due to adsorption to and desorption from the internal surface of the ablation cell. To prevent smearing effects in the images obtained, the signal was allowed to drop back to background levels by waiting several seconds after firing several shots at the same position before interrogating the sample at the next location, drastically increasing the total analysis time. Such smearing effects accompanying these long SPR profiles were also observed in Van Helden *et al*. [33]

The increasing interest in fast elemental mapping is accompanied by the development of more efficient low-dispersion ablation cells [34-37] and faster aerosol transport systems [38, 39], providing single pulse response (SPR) profiles, *i.e.* the transient signal monitored upon an individual laser pulse, with a duration of < 10 ms (FW0.01M, full peak width at 1% of the maximum peak height). The fastest setups can even provide sub-ms SPR durations, paving the way to kHz pixel acquisition rates [37, 38]. Despite these technological improvements, analyses would still have to be slowed down when dealing with elements that are completely or partially transported in gaseous phase. Fractional transport in gaseous phase would result in split or double peaks in the SPR profile. A more elegant approach would consist of preventing or minimizing the generation of analytes in gaseous phase to such an extent that fast mapping conditions can be maintained.

Recent works in which double peaks were observed for Zn, As, Se and Te in the SPR profiles upon ablation of gelatin and mushroom tissue with a low aerosol dispersion LA-setup triggered the in-depth evaluation of gaseous phase formation reported on in this paper, as the selection of instrument settings and data acquisition conditions for elemental mapping via LA-ICP-MS needs specific attention in this case [33, 40]. Using gelatin as a viable substitute for soft biological tissue [41], this work presents a fundamental study focused on evaluating the two-phase sample transport for a wide range of elements upon ablation using 193 nm and 213 nm nanosecond laser radiation.

2. Materials and Methods

2.1 Reagents

Solutions containing 10% (m/m) gelatin (VWR International, Leuven, Belgium) were prepared using ultra-pure milli-Q water (resistivity ≥ 18.2 MΩ cm at 25 °C) in 1.5 mL Eppendorf tubes (Eppendorf, Hamburg, Germany) and were spiked to a final concentration (before drying) of 10 µg g^{-1} of the following elements: Ag, Al, Ba, Cd, Co, Cr, Cu, Eu, Fe, I, In, Mg, Mn, Na, Ni, Pb, Sm, Sr, Tl, U, Zn (Inorganic Ventures, Christiansburg, VA, USA), As, Hg, Te (SCP Science, Villebon-sur-Yvette, France) and Se (Chemlab, Zedelgem, België). The gelatin mixture was heated at a temperature of 55 °C for 1 h, and after homogenization by vortex mixing, droplets of approximately 1 g were spotted on a Superfrost™ soda-lime-silica glass microscope slide (Thermo Fisher Scientific, Waltham, MA, USA), dried at a temperature of 95 °C for 1 h and slowly cooled to room temperature according to the protocol described by Šala *et al.* [42] to achieve homogeneous gelatin droplet standards.

2.2 Fast LA-ICP-TOF-MS multi-elemental mapping of kidney tissue

To showcase the problem related to two-phase sample transport and the effect it can have on the quality of elemental maps generated on biological tissue samples via LA-ICP-MS, a

143 multi-elemental LA-ICP-TOF-MS experiment was performed using an ultra-fast LA-ICP-MS
144 setup consisting of the Iridia LA-system (Teledyne Photon Machines, Bozeman, MT, USA),
145 equipped with a liquid water-cooled MLI-1000 nanosecond 193 nm ArF*excimer-based lasing
146 system (MLase, Germering, Germany) and a Cobalt ablation chamber with tube-type ablation
147 cell [35, 36]. This system was connected to an icpTOF 2R ICP-MS unit (TOFWERK, Thun,
148 Switzerland) via an ARIS (Aerosol Rapid Introduction System [38], Teledyne Photon
149 Machines). PEEK tubing with an ID of 0.75 mm and a length of 45 cm was used to connect
150 both instruments. Kidney tissue intended for fast multi-elemental mapping originated from
151 an earlier study [43], during which animals were exposed to different pharmacological doses
152 of cisplatin (Pt-based chemotherapeutic compound), and was formalin-fixed in 10% neutral
153 buffered formalin and paraffin-embedded. The kidney tissue was sectioned into 5 µm thin
154 sections and placed on Superfrost™ SLS glass microscope slides. The samples were
155 deparaffinized prior analysis and air-dried. The mapping experiments were performed using
156 a laser repetition rate of 250 Hz, energy density of 0.60 J cm^{-2}, a circular spot with a diameter
157 of 5 µm and a dosage of 1.

158 **2.3 LA-ICP-TOF-MS for multi-element determination of single pulse response profiles in**
159 **gelatin**

160 A similar set-up as described above but this time with a cup-type ablation cell, to allow the
161 use of > 10 µm diameter spot sizes, was employed to determine the SPR profiles of a range of
162 elements upon ablation of gelatin standards as proxy for soft biological tissue. PEEK tubing
163 with an ID of 1 mm and a length of either 45 or 90 cm was used to connect both units. The
164 instrument settings were tuned on a daily basis upon ablation of NIST SRM 612 glass reference
165 material (Trace elements in glass, National Institute of Standards and Technology,
166 Gaithersburg, MD, USA), aiming at high sensitivity across the elemental mass range (based on
167 $^{7}Li^{+}$, $^{115}In^{+}$ and $^{238}U^{+}$), low oxide formation ($^{232}Th^{16}O^{+}/^{232}Th^{+}$ < 0.5%) and low laser-induced
168 elemental fractionation ($^{238}U^{+}/^{232}Th^{+} \approx 1$). Using this setup, either gelatin droplets or NIST SRM
169 612 glass were ablated according to a line scan with a circular laser spot size of 20 µm
170 diameter, energy density 3.64 J cm^{-2} and laser repetition rate of 1 Hz. The SPR profiles were
171 calculated (averaged) based on a total of 100 pulses. All instrumental parameters used
172 throughout this work are summarized in the supplementary information (table S1).

173 **2.4 Separation of gaseous and particulate phases using a filter in the transfer line**

174 To verify whether elements were transported in gaseous phase, and if so, which part of the
175 multimodal SPR corresponded to the gaseous phase, experiments were performed in which
176 a PTFE filter with a pore size of 0.1 µm (Cytiva, Marlborough, MA, USA) was fitted into the
177 PEEK tubing connecting the LA unit to the ICP-MS instrument for filtering particles out of the
178 ablation-generated sample aerosol. For these experiments, an Analyte G2 (Teledyne Photon

179 Machines, Bozeman, MT, USA) LA-unit equipped with a liquid-cooled ATLEX-500-I
180 nanosecond 193 nm ArF*excimer-based lasing system (ATL Lasertechnik GmBh,
181 Wermelskirchen, Germany) and a HelEx-II ablation cell was coupled to an Agilent 7900
182 quadrupole-based ICP-MS instrument (Agilent Technologies, Tokyo, Japan). The filter was
183 installed by cutting the PEEK tubing about halfway and fitting connecting pieces to both ends
184 of the cut (Figure S1). These ends could be reconnected with or without a filter present, thus
185 avoiding the effect of other factors which might affect the SPR profile and permitting focusing
186 exclusively on the effect of the filter. Gelatin was ablated based on line scanning with a spot
187 size of 50 µm and a laser repetition rate of 2 Hz. In order to obtain a sufficient fraction of the
188 element of interest in gaseous phase to be able to determine the effect caused by the
189 presence of a filter, an energy density of 2.5 J cm^{-2} was used. The SPR profiles were calculated
190 based on a total of 100 pulses.

191 **2.5 Separation of gaseous and particulate phases using a cryotrap in the transfer line**

192 To further confirm which part of the multimodal SPR corresponds to the gaseous phase and
193 which to the particulate phase, experiments were performed using a cryotrap in an attempt
194 to remove the gaseous phase from the sample aerosol. An Analyte G2 LA-unit equipped with
195 a HelEx-II ablation cell was coupled to an Agilent 7900 quadrupole-based ICP-MS instrument
196 via a short plastic tube, which was placed in a 0.5 L Dewar flask filled with liquid nitrogen to
197 adequately cool down sample aerosol during the transfer from the LA-unit to the ICP. In
198 addition, a PTFE filter with a pore size of 0.1 µm could also be fitted into the tubing, preceding
199 the part placed in the Dewar flask. All four combinations with/without filter and with/without
200 cooling were evaluated. Gelatin was ablated based on line scanning with a spot size of 50 µm
201 and a laser repetition rate of 2 Hz. In order to obtain a sufficient fraction of the element of
202 interest in gaseous phase to be able to accurately determine the effect caused by the
203 presence of the filter and/or cryotrap, an energy density of 4.0 J cm^{-2} was used. SPR profiles
204 were calculated based on a total of 100 pulses.

205 **2.6 Effect of laser energy density on the degree of element-specific gaseous phase**
206 **formation**

207 After verification that the two peaks in the bimodal SPRs are the result of the occurrence of
208 two different phases, a particulate and a gaseous one, that are temporally resolved from one
209 another during aerosol transport from the ablation site to the ICP ion source, an experiment
210 was performed to evaluate the effect of the laser energy density on the degree of gaseous
211 phase formation. For this purpose, gelatin was ablated according to a series of line scans at
212 different laser energy densities, ranging from 0.07 to 6.30 J/cm^2, using an Iridia LA-system
213 equipped with a Cobalt ablation chamber and cup-type ablation cell, coupled to an icpTOF 2R
214 ToF-based ICP-MS unit via the ARIS and PEEK tubing. The laser beam path was equipped with

dual attenuators to precisely modulate the laser energy density over a wide range. For all line scans, a laser spot size of 20 µm, repetition rate of 1 Hz and dosage of 5 was used. For every condition, the corresponding SPR profile was calculated based on the average of 100 pulses.

2.7 Effect of laser wavelength on the degree of gaseous phase formation (193 vs 213 nm)

The effect of laser wavelength on the formation of gaseous species was evaluated by carrying out an identical set of experiments using two different laser systems: an LSX-213 G2+ (Teledyne Photon Machines, Bozeman, MT, USA), with a solid-state Nd:YAG laser working at its fifth harmonic wavelength of 213 nm, and an Analyte G2 with an ArF* excimer-based laser unit working at its fundamental wavelength of 193 nm. Both systems were equipped with a HelEx-II ablation cell and coupled to an Agilent 7900 ICP-MS unit via the ARIS and PEEK tubing with an ID of 1 mm and a length of 2 m for the 213 nm system and 2.5 m for the 193 nm system. Long tubing was selected with the intention to separate the two phases sufficiently from one another, thus allowing for adequate integration of both corresponding peaks.

Using both setups, gelatin was ablated according to a series of line scans with a spot size of 20 µm, a repetition rate of 1 Hz with the LSX-213 G2+ and 2 Hz with the Analyte G2 LA unit and an energy density of 0.82 to 4.89 J cm^{-2} with the LSX-213 G2+ and 0.50 to 5.0 J cm^{-2} with the Analyte G2. The nuclides monitored are $^{13}C^+$, $^{63}Cu^+$, $^{66}Zn^+$, $^{82}Se^+$, $^{88}Sr^+$, $^{125}Te^+$ and $^{208}Pb^+$, and for every nuclide, for every measured energy density, one line scan of 100 pulses was performed to determine the average SPR.

2.8 Data processing software

Various software packages were used throughout this work. HDIP (version 1.7.1, Teledyne Photon Machines, Bozeman, MT, USA) was used to synchronize the ICP-MS data files to the laser log files and the peak detection tool was used to extract average peak profiles. A combination of in-house developed Matlab scripts (version 9.11) and Microsoft Excel was used to further process the spectral data, perform background corrections, peak detection and integration. All plots and graphs were made using Matlab, and were further modified using Paint.net.

3. Results & Discussion

3.1 Fast LA-ICP-TOF-MS multi-elemental mapping of kidney tissue

A radial segment of a kidney tissue section was analyzed using a fast LA-ICP-TOF-MS setup in a spot-resolved manner to illustrate the effect of element-specific two-phase sample transport on the quality of elemental maps. The instrument settings and data acquisition conditions were selected based on the short SPR profiles obtained for ^{195}Pt (typically < 3 ms).

The multi-elemental maps are displayed in Figure 1 and demonstrate good image quality for ^{23}Na, ^{31}P, ^{56}Fe and ^{195}Pt as the walls of the renal tubules, the pipe-like structures through which the primary urine flows, are clearly defined. In contrast, the maps for ^{32}S, ^{127}I and to some extent ^{66}Zn, show significant smearing as the individual renal tubular structures cannot be identified anymore.

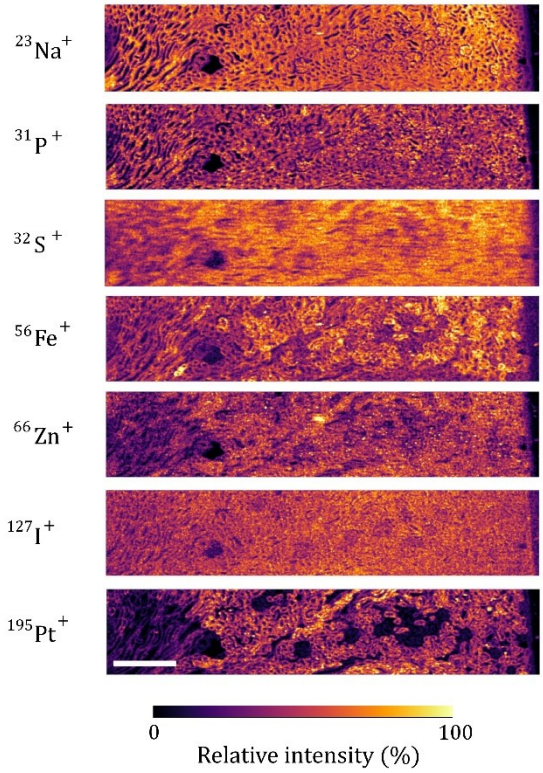

Figure 1. 2D multi-elemental LA-ICP-TOF-MS maps obtained upon analysis of a radial segment of kidney tissue using a fast LA setup. The color bar corresponds to the relative intensity per nuclide. The white scale bar corresponds to 500 µm.

As each pixel contains information on all elements measured quasi-simultaneously for each individual laser pulse, these results clearly illustrate that while the chosen measurement parameters are appropriate for some elements, they are not for others. These results match those of Van Helden *et al.* [33], where the hypothesis was put forward that this behavior is caused by the formation of two phases upon ablation for some elements, which are visible as two peaks in the SPR profiles. It is further said that as these phases are separated from each other in the tubing connecting the ablation chamber to the ICP, the total duration of the SPR profile can increase to such an extent that smearing occurs, when the instrument settings and data acquisition conditions are not appropriately adjusted.

3.2 LA-ICP-TOF-MS for multi-element determination of SPR profiles

To determine for which elements a significant gas phase was formed upon ablation of a multi-element spiked gelatin droplet standard, an Iridia LA-system was coupled to a quasi-simultaneous monitoring ICP-TOF-MS instrument. Individual peak profiles were monitored for a large collection of elements while ablating at low laser repetition rate (1 Hz). With this approach, SPR profile shapes and integrated areas under the peak can be compared, while also the respective arrival times of the two different phases (corresponding to different peaks in the SPR profile) for all the elements of interest (24) can be documented. The same experiment was performed using NIST SRM 612 glass reference material to evaluate the possible occurrence of a gas phase for the same set of elements.

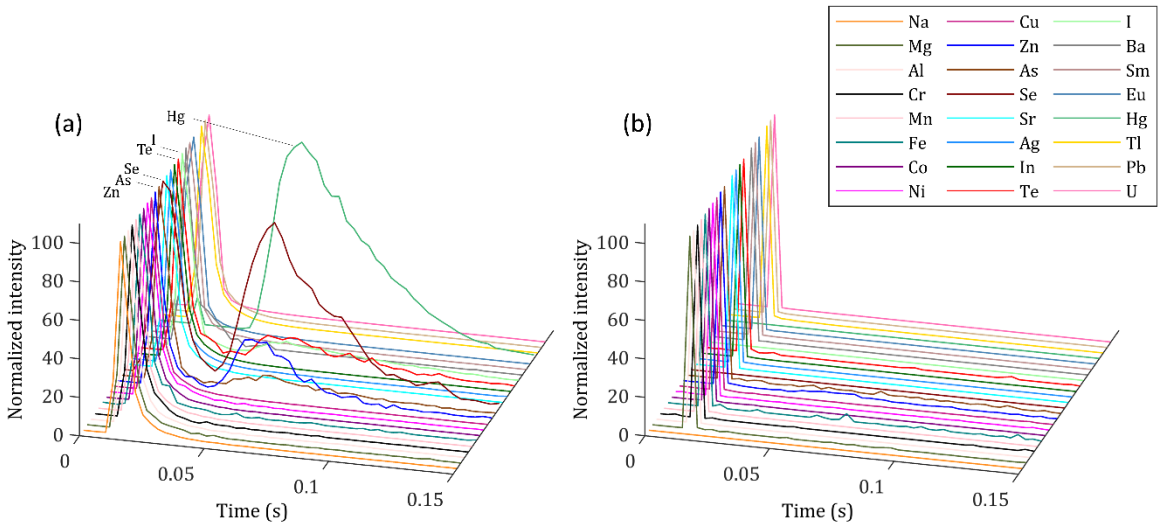

Figure 2. Average SPR profiles (N = 100) obtained with a combination of an Iridia LA-system coupled to an ICP-TOF-MS unit upon ablation of (a) gelatin and (b) NIST SRM 612 glass. The ablation cell was connected to the ARIS mixing bulb using 90 cm PEEK tubing. All line scans were ablated at low repetition rate using a circular laser spot size of 20 µm diameter and a laser energy density of 3.64 J cm^{-2}. Elements showing significant gas phase formation upon ablation of gelatin are Zn (blue), As (saddle brown), Se (maroon), Te (red), I (pale green) and Hg (medium sea green).

The SPR profiles in Figure 2a illustrate that based on all nuclides monitored, the elements can be divided into three distinct groups: a group showing one, narrow peak in the SPR profile only (such as Al, Cu, In, Pb and U), a group with one, wide peak in the SPR profile only, (such as Hg), and a group of elements that show a bimodal SPR profile with two temporally separated peaks (such as Zn, As, Se, Te and I).

Figure 2b shows SPR profiles obtained upon ablation of NIST SRM 612 glass. For every element, the SPR profile shows one narrow peak only. As figures 2a and 2b were obtained

under exactly the same lasing conditions and using the same setup, these results illustrate the matrix-specific behaviour of the two-phase transport. This further emphasizes that in the context of mapping experiments it is essential to determine the actual SPR duration for a specific matrix and match the acquisition parameters accordingly. If the SPR profile for an element in a glass reference material is used to select the acquisition parameters to be used for mapping the distribution of elements in soft biological tissue, the final image could show significant smearing effects since typically the maximum achievable pixel acquisition rate will be overestimated.

Figure S2 shows SPR profiles obtained under the same conditions as in figure 2a, except for changing the transport tubing length from 90 cm to 45 cm. It was previously observed that shortening the tubing reduces the gap in arrival time between the two peaks/phases for Se [33]. The results obtained here confirm this: the difference in arrival time between the two peaks (maxima) was 45 ms with the 90 cm tubing and 24 ms with the 45 cm tubing. The correlation between tubing length and difference in arrival time is nearly linear, thus implying that the separation between these two phases occurs almost exclusively in the transport tubing, and not in the ablation cell. The separation between the two peaks could also be reduced by increasing the total He carrier gas flow rate: from 44 ms at 0.2 L min^{-1} to 20 ms at 0.6 L min^{-1}. These results indicate that the two peaks originate from different phases which travel independently from each other from the ablation chamber to the ICP, and that all elements transported in one specific phase will be transported in the same manner. In addition, these results suggest that it is possible to reduce, but never eliminate, the separation between the two peaks using the PEEK transport tubing, since transport tubing of some length will always be necessary.

3.3 Separation of gaseous and particulate phases using a filter in the transfer line

To investigate which phase each peak within the bimodal SPR profile corresponds to, an experiment was performed in which a filter was placed into the PEEK tubing connecting the HelEx-II ablation chamber of the Analyte G2 LA unit to the ARIS mixing bulb. All connection pieces were fitted in such a way that the filter could be placed and removed easily, so that only the effect of the presence of the filter could be evaluated. For these experiments, a quadrupole-based ICP-mass spectrometer (Agilent 7900) was used and multiple nuclides were monitored sequentially in individual runs.

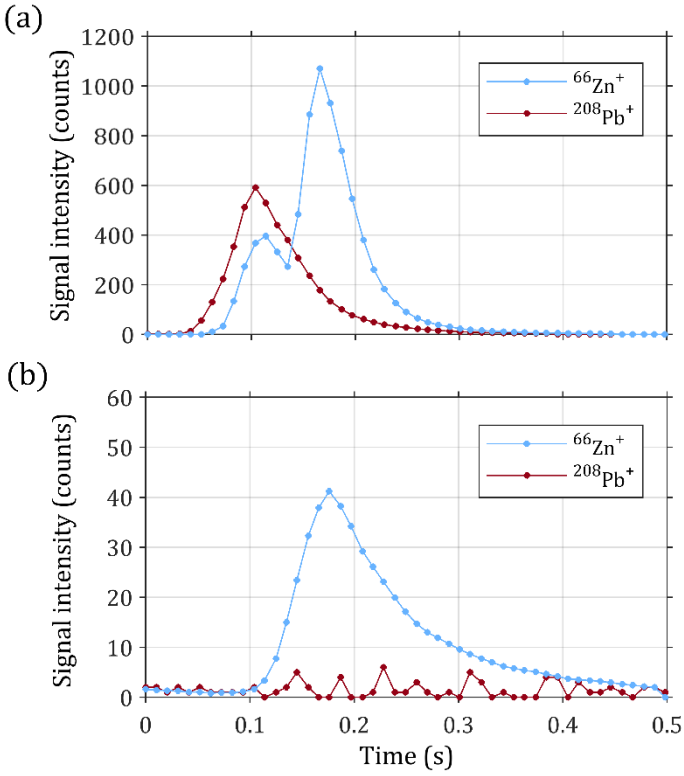

Figure 3. Average SPR profiles for $^{66}Zn^{+}$ and $^{208}Pb^{+}$ obtained upon ablation of gelatin (N = 100) (a) without filter and (b) with 0.1 µm PTFE filter fitted into the PEEK tubing.

Figure 3a shows the average SPR profiles obtained upon ablation of a multi-element spiked gelatin droplet standard without the actual filter installed, but including the connection pieces. These additional parts resulted in a slight dead volume, giving rise to turbulences and an increase of the total SPR duration from approximately 25 to 125 ms for ^{208}Pb (FW0.1M, full peak width at 10% of the maximum peak height). However, the SPR profile for ^{66}Zn still shows two distinct peaks, and that of ^{208}Pb a single peak only, consistent with the results obtained using the "standard" setup as discussed in the previous section. After installing a 0.1 µm pore size PTFE filter in the transfer line, the SPR profiles changed significantly, as shown in Figure 3b. For ^{66}Zn, only one of the two peaks remains, while for ^{208}Pb, the signal is reduced to approximately background levels. Since filtering is intended to remove the particulate phase, and one peak is fully eliminated for both elements, these findings seem to suggest it is the first peak in the upper pane which corresponds to sample material transported in particulate phase, while the second peak corresponds to material converted into gaseous phase, which is in line with the hypothesis put forward in a previous work [33]. The ^{66}Zn peak maximum is significantly lower with the PTFE filter in the transfer line but this can be attributed to peak broadening and potentially some losses due to metal vapor condensation on the PTFE filter.

3.4 Separation of gaseous and particulate phases using a cryotrap in the transfer line

To conclusively verify these findings, an additional experiment was performed in which the opposite approach was evaluated: instead of removing the particulate phase using a filter, a cryotrap was used with the intention of removing the gaseous phase from the sample aerosol during its transport to the ICP ion source. The motivation behind this experiment is that as the gas phase is sufficiently cooled down, it will lead to vapor deposition on the internal surface of the transport tubing, which will result in the second peak being partially or completely removed from the SPR profile.

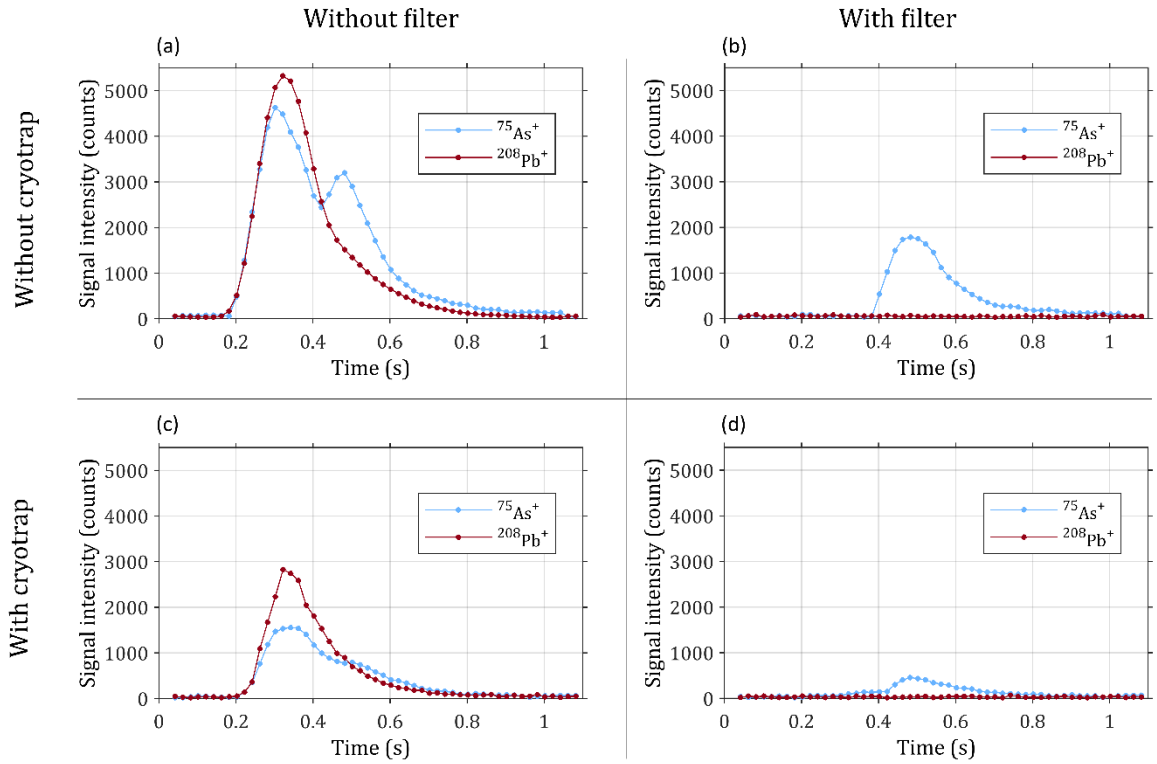

Figure 4. Average SPR profiles for $^{208}Pb^+$ and $^{75}As^+$ upon ablation of gelatin (N = 100). (a) Profiles obtained using the standard setup. (b) Profiles obtained with a 0.1 µm PTFE filter fitted into the tubing. (c) Profiles obtained with the tubing passed through a liquid N_2 cryotrap (no filter present). (d) Profiles obtained with a 0.1 µm filter fitted into the tubing, and the tubing passed through a liquid N_2 cryotrap.

Figure 4a shows the average SPR profiles for ^{208}Pb and ^{75}As, using the standard LA-ICP-MS setup. Upon introducing a filter in the tubing (Figure 4b), the particulate phases of Pb and As are removed, and only the gaseous phase of As is remaining. When the tubing is passed through a cryotrap, the second peak in the As profile almost completely disappeared from the SPR profile, as shown in Figure 4c, indicating that this peak corresponds to the gaseous phase formed upon ablation. The ^{208}Pb and ^{75}As peak maxima are reduced for both particulate phases as a results of peak broadening and potentially, some particle losses due to coiling of

the tubing in the cryotrap. Finally in Figure 4d, when both a cryotrap and filter are placed in the line, almost all signal is removed, only a small fraction of the second peak of As remains visible. By comparing the integrated intensities for the peaks of As in Figure 4b and 4d, the efficiency of the cryotrap was calculated to be 76%.

3.5 Effect of laser energy density on the degree of element-specific gaseous phase formation

3.5.1 Carbon

Subsequent experiments were performed using ICP-Q-MS to assess the effect of laser energy density upon the formation of gas phase. Since carbon has already been studied extensively in this context [28, 30], our starting point consisted of determining SPR profiles for C at various energy densities. For every SPR profile obtained, the SPR peaks corresponding to particulate and gaseous phase were separately integrated and the ratio *versus* the total integrated signal intensity was calculated for both peaks. The figure below summarizes these intensity ratios for both the gaseous and the particulate peak vs the total (integrated) intensity as a function of the energy density for ^{13}C.

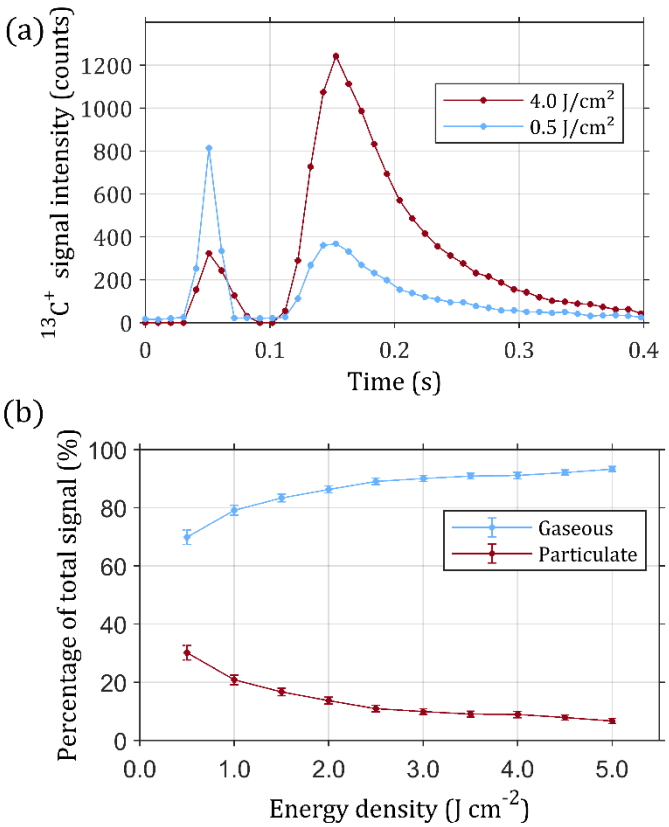

Figure 5. (a) Average SPR profiles (N = 100) for $^{13}C^+$ upon ablation of gelatin at two energy densities. (b) The fraction of the total integrated signal intensity (entire SPR profile)

381 represented by the particulate (red) and gaseous (blue) phases of $^{13}C^{+}$ is plotted against the
382 energy density.

383 Figure 5 shows a clear trend towards more gas phase as the laser energy density increases.
384 Initially, there is a relatively steep increase in the fraction of gas phase, which plateaus to a
385 constant value of approximately 90% at higher energy densities. As porcine skin gelatin
386 displays a stoichiometric oxygen/carbon ratio of approximately 0.32, this value corresponds
387 relatively well to the fraction of gaseous phase C that could be expected for this type of
388 biological material according to a previous work of Frick and Günther [28, 44].

389 3.5.2 Multi-element SPR monitoring using ICP-TOF-MS

390 A similar experiment was performed using ICP-TOF-MS and multi-element gelatin droplets to
391 characterize the effect of energy density (0.07 – 6.30 J cm^{-2}) on gaseous phase formation for
392 a wide range of elements (Figure 6).

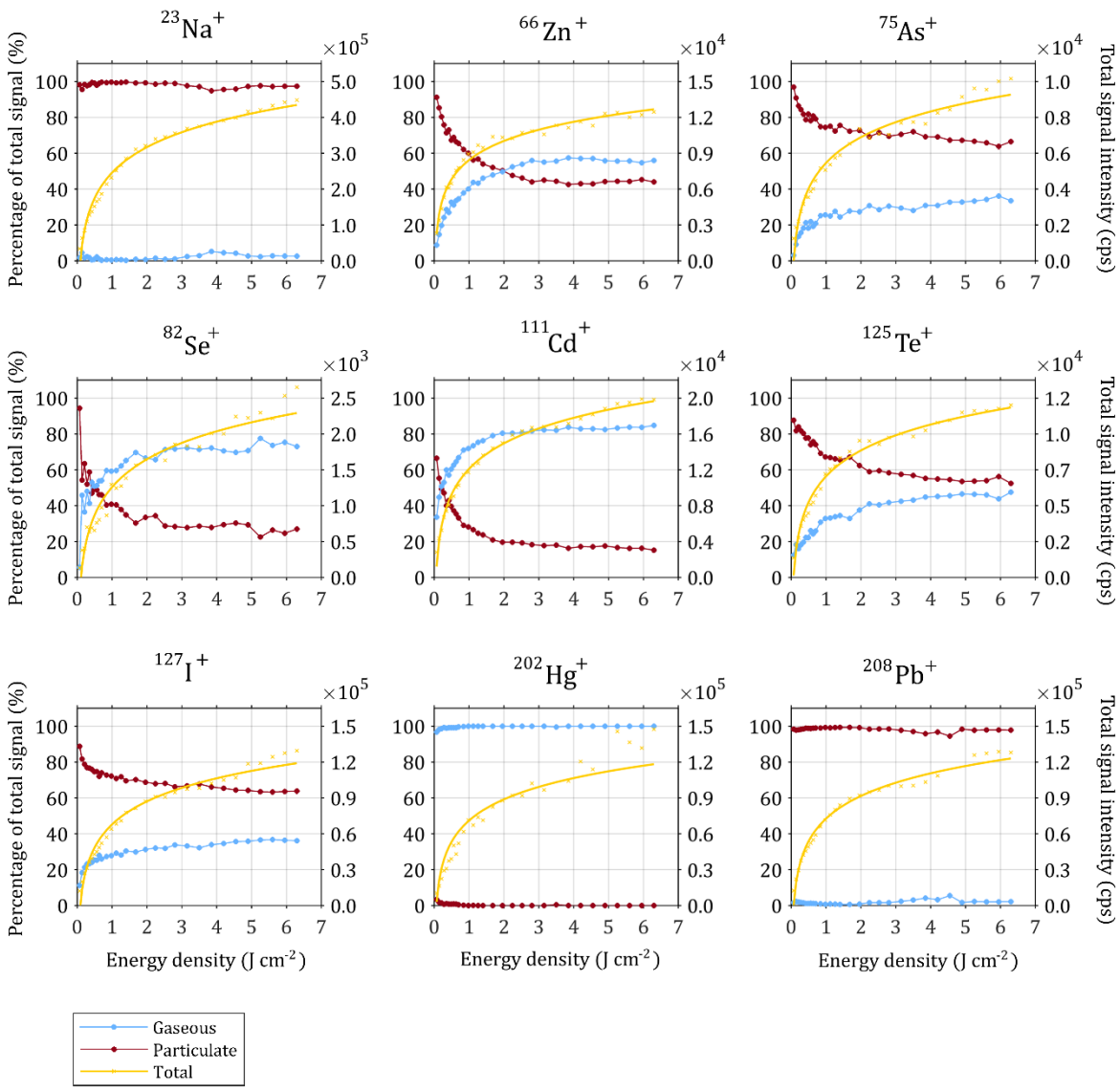

Figure 6. On the left y-axis, the percentage of the total integrated signal intensity of the entire SPR profile represented by the particulate (red) and gaseous (blue) phases is plotted against the laser energy density for 9 nuclides. The right y-axis shows the total integrated signal intensity of both phases combined (yellow), expressed in counts per second.

For all elements that are transported in two phases, there is a logarithmic trend of the fraction transported in the gas phase as a function of the laser energy density, levelling off (plateauing) at higher energy densities. This behaviour appears to be strongly element-specific, as the plateau reached and the slope of the logarithmic part leading up to the plateau are different for all elements monitored. The exact reason for this element-specific behaviour has not yet been revealed. An attempt was done to find a correlation between this behaviour and several physico-chemical characteristics of the elements. Since all elements for which this behaviour was observed are volatile, the parameters investigated include boiling point, sublimation

enthalpy and 50% condensation temperature (i.e., the temperature at which 50% of the total amount of a specific element would condense from a vapour) [45], but no quantitative relationship was revealed for any of these parameters that would fit all elements. In this context, it is important to point out that various elements might not be transported in the same chemical form. For instance, it has been reported that C is transported as CO_2 [28], while other elements might be transported in a different form, such as an elemental gas, e.g. Hg [46], a volatile hydride or alkylated species, e.g. As [47], or even a combination of different forms [48]. Because of this, multiple physico-chemical properties could govern the degree to which an element is transported in gaseous phase, and further work focusing on identification of the chemical species involved could further shed light on this issue. For all nuclides monitored, the total integrated signal intensities seem to follow a highly similar logarithmic trend with increasing laser energy density, with the same general shape, suggesting no significant diffusion losses for elements partially or fully transported in the gaseous phase. The curves depicted in Figure 7 show the integrated signal intensity of the gaseous and particulate peaks, and of the total SPR profile. Since no gaseous peak is present for ^{23}Na, the total integrated signal intensity is quasi-identical to that of the particulate peak. On the other hand, the signal intensities of the particulate peaks of ^{111}Cd and ^{66}Zn plateau already at low energy densities (0.5-1 J cm^{-2}), while this is not the case for ^{23}Na.

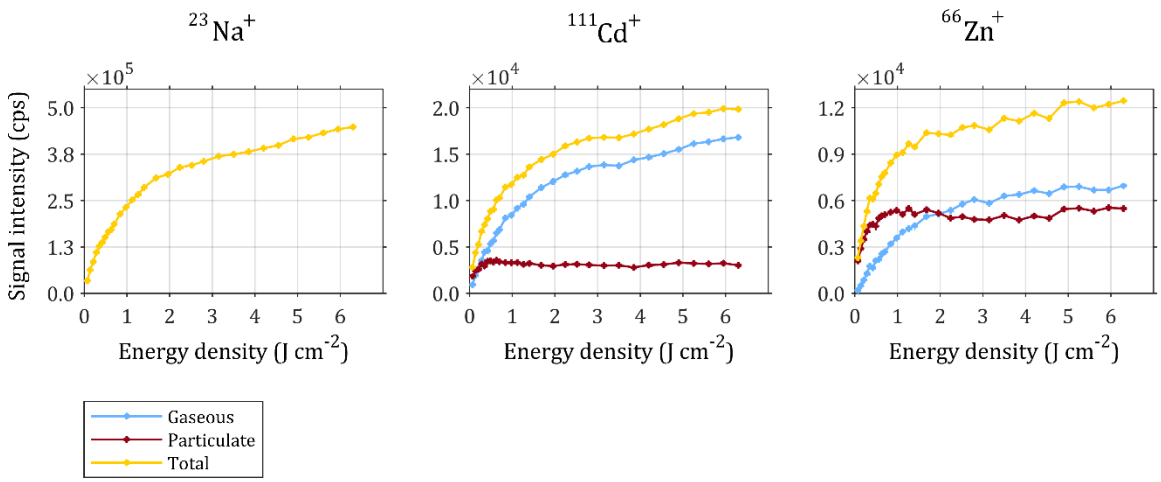

Figure 7. Integrated signal intensities of the gaseous peak (blue), particulate peak (red) and total SPR profile (yellow) plotted as a function of the laser energy density for $^{23}Na^+$, $^{111}Cd^+$ and $^{66}Zn^+$.

When the integrated signal intensity of the total SPR profile is normalized to that of $^{23}Na^+$, a difference appears between the elements transported in one phase, in comparison to those transported in two phases. For all elements transported in both the gaseous and particulate phase, except for Se, plotting the normalized integrated signal as a function of laser energy

density reveals a sharp drop at low laser energy densities, while the for elements transported in a single phase, such as Ni and Cr, the normalized signal intensities remain constant (Figure 8a). When the normalized intensities are plotted as a function of the fraction of the nuclide transported as gas phase (Figure 8b), a linearly decreasing trend can be observed for every nuclide, but Se. This indicates that as the amount of gaseous phase increases for every element but Se, the signal intensities obtained for such element will decrease relative to that for elements transported in one phase only, such as Na.

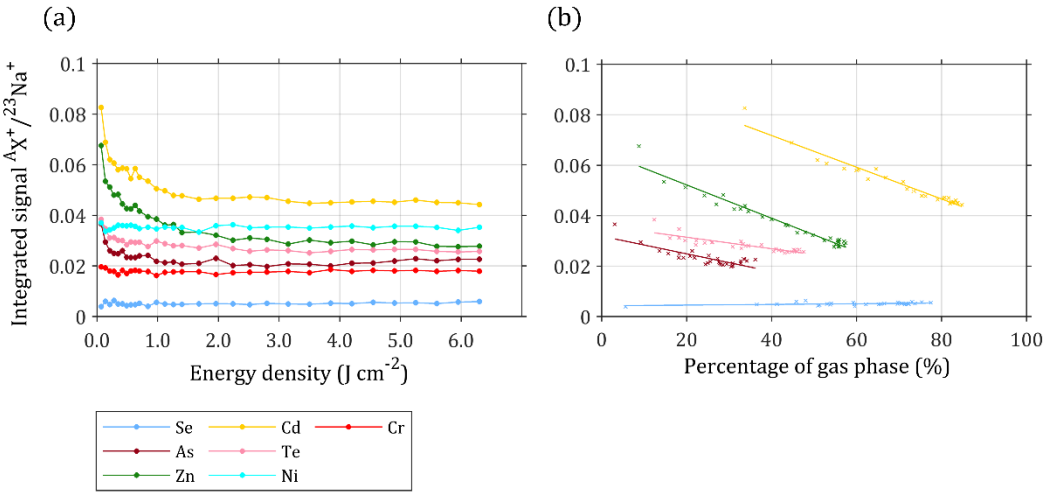

Figure 8. Integrated signal intensities for various nuclides normalized to the integrated signal of $^{23}Na^{+}$ (a) as a function of laser energy density and (b) as a function of the percentage of the element transported in the gas phase.

It is hypothesized that the origin of this behaviour lies in the difference in the transport to and ionization in the ICP between gaseous and particulate material. Typically, the instrument is tuned based on the signal intensities of various elements, such as Co, In and U, usually upon ablation of a glass reference material. As a consequence, the instrumental performance is optimized for particles, and not gases. In contrast to particles which firstly are subjected to a vaporization step, the gaseous phase will directly undergo the atomization and subsequent ionization processes. For gases, the maximum ion density can be located more upstream in the ICP relative to the maximum ion density for particles, which would mean that this zone may be less well positioned relative to the sampling cone, resulting in less efficient extraction of the ions at that location, leading to a reduction in signal intensity [49]. When measuring elements which are prone to forming a gas phase, this will result in a relative loss in sensitivity in comparison to elements only transported in the particulate phase. Since the amount of gas phase increases as the laser energy density increases, this effect will become more apparent at higher energy densities.

3.6 Effect of laser wavelength on the degree of gaseous phase formation (193 vs 213 nm)

3.6.1 Comparison of the laser energy density effect on gaseous phase formation for 193 and 213 nm laser radiation

For assessing the influence of the wavelength, two almost identical set-ups except for the lasers were used. An Analyte G2 equipped with a 193 nm ArF*excimer laser unit was used at Ghent University, while an LSX-213 G2+ unit was used at the University of Zagreb. Both LA-units were equipped with the same ablation cell and aerosol transport system. An Agilent 7900 quadrupole-based ICP-MS unit was selected for signal monitoring as such instrument was available at both locations and this selection secured further similarity between both set-ups, thus "isolating" wavelength as the parameter studied.

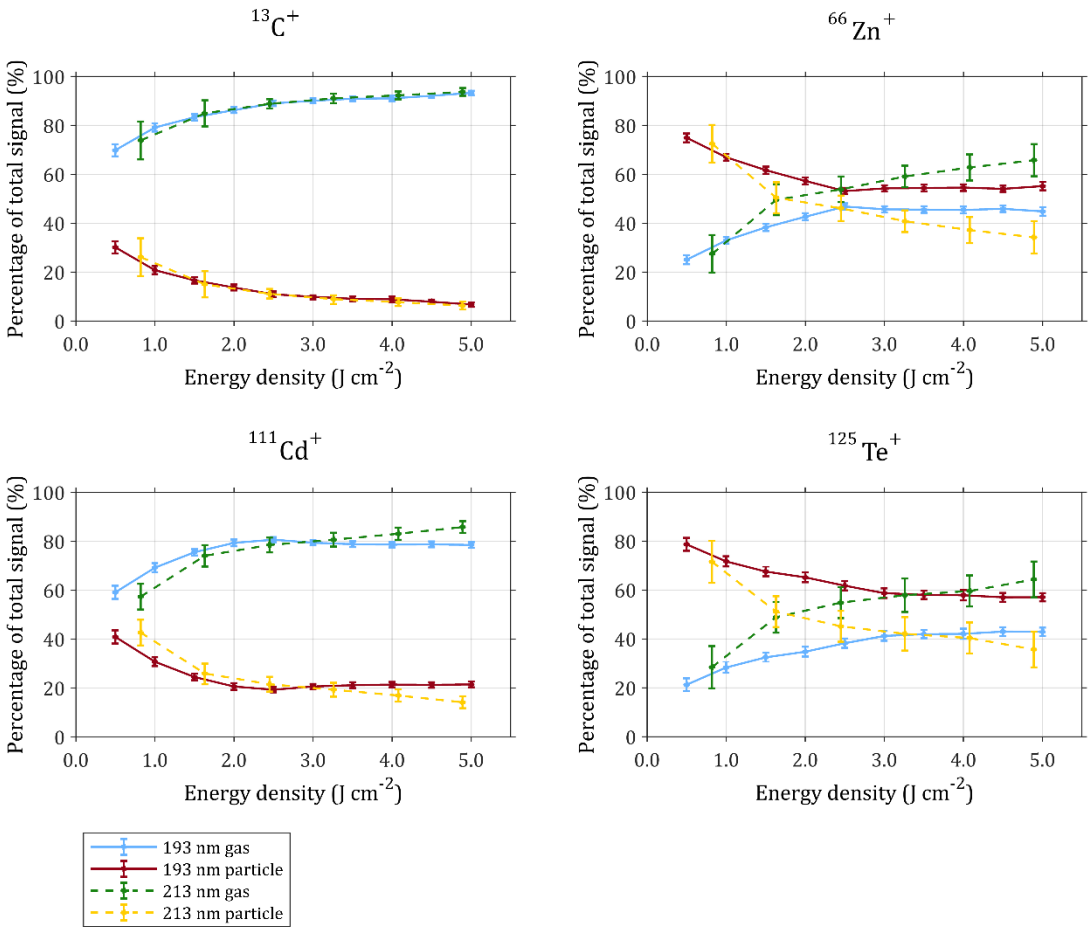

Figure 9. The fraction of the total integrated signal intensity of the entire SPR profile represented by the particulate and gaseous phases is plotted against the energy density for four elements, for both a 193 nm ArF*excimer laser and a 213 nm Nd:YAG laser. Results are shown for $^{13}C^+$, $^{66}Zn^+$, $^{111}Cd^+$ and $^{125}Te^+$. Error bars represent the SD.

Figure 9 shows the fraction transported as gaseous or particulate phase *versus* the laser energy density for $^{13}C^+$, $^{66}Zn^+$, $^{111}Cd^+$ and $^{125}Te^+$ at both 213 and 193 nm. The error bars represent the standard deviation, based on 100 individual ratios. It can be observed that the standard deviations for the datapoints obtained at 213 nm are significantly higher than those at 193, due to lower sensitivity, but the general trends of the curves can be compared.

Earlier in this work, it was mentioned that the gas-phase fraction varies as a function of the laser energy density in an element-specific manner (section 3.4.2), but it appears that also the influence of laser radiation wavelength on the corresponding curve is unique to each element. For instance, the curves for ^{13}C obtained at 193 nm and 213 nm seem to overlap: both curves plateau at a value of about 95%, and the initial increase in gas fraction at lower energy densities follows the same trend for both wavelengths. Conversely, for both ^{66}Zn and ^{125}Te, there is a significant difference between the curves obtained using the 193 nm and 213 nm lasers: for both these elements the fraction of gaseous phase reaches a plateau at around 43% with the 193 nm laser, and at approximately 75% with the 213 nm laser. Especially at lower energy densities, an increase in laser energy density leads to a steep increase in the gas fraction with the 213 nm laser. The impact of the wavelength on the behaviour of Cd is still observable, although to a lesser degree, exhibiting a behaviour that is intermediate between C and Zn/Te. A general conclusion that can be drawn is that when the wavelength is increased from 193 to 213 nm, either the same or a higher extent of gas phase formation is observed.

A possible explanation for this behaviour could lie in the extent to which thermal effects are induced by the photon beam. Sutcliffe and Srinivasan [50] have reported that at 193 nm, only a small fraction of the energy will be transformed into heat, whereas for longer wavelengths, up to 100% of the energy would be transformed into heat. While their study was conducted on PMMA, it is stated that the general trend of this behaviour, i.e. more thermal effects with increasing wavelength, would be valid for biological tissue as well, although this should be investigated and verified in depth in a dedicated study.

3.6.2 Comparison of SPR profiles for 193 and 213 nm laser radiation

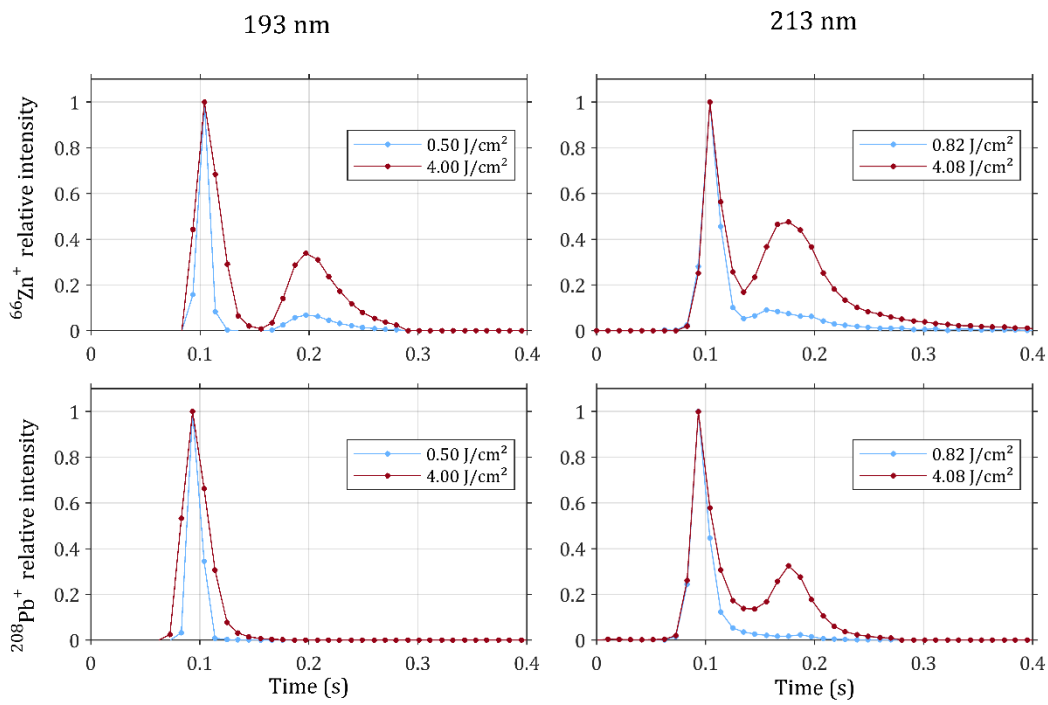

Figure 9. SPR profiles for $^{66}Zn^+$ (top) and $^{208}Pb^+$ (bottom) obtained upon ablation of gelatin by laser radiation with a wavelength of 193 nm (left) or 213 nm (right). For all four conditions, the SPR profiles were obtained at both a low or a high energy density: 0.5 (blue) and 4.0 (red) J cm^{-2} for 193 nm and 0.82 (blue) and 4.08 (red) J cm^{-2} for 213 nm.

Figure 9 displays an additional finding observed upon changing the wavelength from 193 to 213 nm. At 193 nm, two distinct peaks, corresponding to the particulate and gaseous phases, are seen for ^{66}Zn, while for ^{208}Pb, only one peak, corresponding to the particulate phase, is present. When increasing the laser energy density from 0.5 to 4.0 J cm^{-2}, the general appearance of the SPR profile (number of peaks) does not change, but the proportion of Zn that is transported in the gas phase increases as previously noted. At 213 nm, however, already at a relatively low laser energy density of 0.82 J cm^{-2}, the SPR profile of Pb shows two peaks, demonstrating that in contrast to the situation at 193 nm, Pb is partly transported in gaseous phase at 213 nm. This effect is even more pronounced when ablating at a higher laser energy density of 4.08 J cm^{-2}. This behaviour in which gaseous phase is formed at 213 nm but not at 193 nm was also observed for the remaining nuclides monitored using this setup: Sr and Cu.

These results are a further proof that appropriate selection of the laser wavelength is also of significant importance for ablation of soft C-based materials. In the past, it has been described that due to the efficient coupling, photon beams with a wavelength around 190 nm are

absorbed well by the protein polypeptide backbone and are therefore very suitable for ablation of soft tissues [51]. Especially since, by carefully selecting the laser energy density, it is possible to selectively ablate tissue sections while avoiding co-ablation of the underlying substrate . This conclusion was based on physical parameters related to the ablation process itself, but by also considering the effect on formation of multiple phases upon ablation, an additional dimension can be added to this reasoning.

4. Conclusions

Single pulse response profiles obtained upon ablation of gelatin as a model for soft biological tissue were studied for a large collection of elements and the influence of various parameters was assessed. For some elements (such as C, Zn, As, Se, Cd, Te and I), bimodal peaks were observed. Results obtained from experiments using a filter to remove particulate matter and using a cryotrap to remove gaseous compounds, support the hypothesis that the two peaks in such SPR profiles are caused by formation of both a particulate and gaseous phase, separated from one another in the aerosol transport tubing connecting the ablation chamber to the ICP torch. Further experiments demonstrated that the relative contribution of these two phases changes as a function of the laser energy density and laser wavelength. Furthermore, by switching the laser radiation wavelength from 193 nm to 213 nm, the SPR profile for some elements (such as Pb, Sr and Cu) indicates that only a particulate phase occurs upon ablation at 193 nm, while at 213 nm a significant fraction is transported in gas phase. Gas phase formation was also shown to be matrix-dependent. For gelatin, significant fractions of specific elements are transported in gaseous phase upon ablation by 193 nm laser radiation, e.g., up to 100% for Hg and up to 80% for Cd. Due to similar ablation behaviour, it is expected that this will be the case for most soft biological tissues for which gelatin is often used as a matrix-matched standard. For NIST SRM 612 glass, however, neither for Hg, Cd nor for any of the other elements investigated, a gas phase was observed.

This work shows that formation of two separate phases upon laser ablation of biological tissues is more common than previously realized. With regards to elemental mapping via LA-ICP-MS, the separation of these two phases in the aerosol transport tubing and corresponding increase in the SPR duration can lead to a significant deterioration of the image quality at high pixel acquisition rates in the form of smearing effects. To maintain a high analysis speed, the problem can be tackled according to a two-fold approach. First, the contribution of the gas peak can be kept to a minimum by reducing the laser energy density. Second, to prevent a large separation between both phases, the carrier gas flow rates can be increased, and short aerosol transport tubing can be used to connect the ablation cell to the ICP torch. However, since this might not always be possible due to the specific layout of the lab or setup, further

research is needed to better understand the origin and identity of these species to further reduce or circumvent the corresponding analytical consequences.

5. Acknowledgements

The authors acknowledge the financial support from the Slovenian Research Agency (research core funding No. P1-0034). TVA thanks Research Foundation – Flanders (FWO) for his junior postdoctoral fellowship grant (FWO.3E0.2022.0048.01).

6. Declaration of competing interest

Tom Van Helden, Thibaut Van Acker, and Frank Vanhaecke conduct research at a research unit that has licensed intellectual property to Teledyne Photon Machines. The other authors have no conflict of interest.

7. References

[1] A.L. Gray, Solid sample introduction by laser ablation for inductively coupled plasma source mass spectrometry, Analyst, 110 (1985) 551-556.

[2] S.E. Jackson, H.P. Longerich, G.R. Dunning, B.J. Freyer, The application of laser-ablation microprobe; inductively coupled plasma-mass spectrometry (LAM-ICP-MS) to in situ trace-element determinations in minerals, The Canadian Mineralogist, 30 (1992) 1049-1064.

[3] B.J. Fryer, S.E. Jackson, H.P. Longerich, The application of laser ablation microprobe-inductively coupled plasma-mass spectrometry (LAM-ICP-MS) to in situ (U)-Pb geochronology, Chemical Geology, 109 (1993) 1-8.

[4] R.J. Watling, H.K. Herbert, D. Delev, I.D. Abell, Gold fingerprinting by laser ablation inductively coupled plasma mass spectrometry, Spectrochimica Acta Part B: Atomic Spectroscopy, 49 (1994) 205-219.

[5] W. Devos, M. Senn-Luder, C. Moor, C. Salter, Laser ablation inductively coupled plasma mass spectrometry (LA-ICP-MS) for spatially resolved trace analysis of early-medieval archaeological iron finds, Fresenius' journal of analytical chemistry, 366 (2000) 873-880.

[6] M. Resano, E. García-Ruiz, F. Vanhaecke, Laser ablation-inductively coupled plasma mass spectrometry in archaeometric research, Mass Spectrometry Reviews, 29 (2010) 55-78.

[7] P. Degryse, F. Vanhaecke, Status and prospects for quasi-non-destructive analysis of ancient artefacts via LA–ICP–MS, Elements, 12 (2016) 341-346.

[8] M. Resano, F. Vanhaecke, D. Hutsebaut, K. De Corte, L. Moens, Possibilities of laser ablation-inductively coupled plasma-mass spectrometry for diamond fingerprinting, Journal of Analytical Atomic Spectrometry, 18 (2003) 1238-1242.

[9] B. Hattendorf, C. Latkoczy, D. Günther, Peer Reviewed: Laser Ablation-ICPMS, Analytical Chemistry, 75 (2003) 341 A-347 A.

[10] R.E. Russo, X. Mao, J.J. Gonzalez, S.S. Mao, Femtosecond laser ablation ICP-MS, Journal of Analytical Atomic Spectrometry, 17 (2002) 1072-1075.

[11] J. Gonzalez, X. Mao, J. Roy, S. Mao, R. Russo, Comparison of 193, 213 and 266 nm laser ablation ICP-MS, Journal of Analytical Atomic Spectrometry, 17 (2002) 1108-1113.

[12] B. Fernández, F. Claverie, C. Pécheyran, O.F. Donard, Direct analysis of solid samples by fs-LA-ICP-MS, TrAC Trends in Analytical Chemistry, 26 (2007) 951-966.

[13] H.-R. Kuhn, M. Guillong, D. Günther, Size-related vaporisation and ionisation of laser-induced glass particles in the inductively coupled plasma, Analytical and Bioanalytical Chemistry, 378 (2004) 1069-1074.

[14] M. Guillong, I. Horn, D. Günther, A comparison of 266 nm, 213 nm and 193 nm produced from a single solid state Nd: YAG laser for laser ablation ICP-MS, Journal of analytical atomic spectrometry, 18 (2003) 1224-1230.
[15] J. Koch, A. Von Bohlen, R. Hergenröder, K. Niemax, Particle size distributions and compositions of aerosols produced by near-IR femto-and nanosecond laser ablation of brass, Journal of Analytical Atomic Spectrometry, 19 (2004) 267-272.
[16] I. Horn, M. Guillong, D. Günther, Wavelength dependant ablation rates for metals and silicate glasses using homogenized laser beam profiles—implications for LA-ICP-MS, Applied Surface Science, 182 (2001) 91-102.
[17] D. Günther, Laser-ablation inductively-coupled plasma mass spectrometry, Analytical and bioanalytical chemistry, 372 (2002) 31-32.
[18] B.S. Luk'yanchuk, W. Marine, S.I. Anisimov, G. Simakina, Condensation of vapor and nanoclusters formation within the vapor plume produced by nanosecond laser ablation of Si, Ge, and C, Laser Applications in Microelectronic and Optoelectronic Manufacturing IV, SPIE, 1999, pp. 434-452.
[19] J. Koch, I. Feldmann, N. Jakubowski, K. Niemax, Elemental composition of laser ablation aerosol particles deposited in the transport tube to an ICP, Spectrochimica Acta Part B: Atomic Spectroscopy, 57 (2002) 975-985.
[20] H.-R. Kuhn, D. Günther, Elemental fractionation studies in laser ablation inductively coupled plasma mass spectrometry on laser-induced brass aerosols, Analytical Chemistry, 75 (2003) 747-753.
[21] A. Limbeck, P. Galler, M. Bonta, G. Bauer, W. Nischkauer, F. Vanhaecke, Recent advances in quantitative LA-ICP-MS analysis: challenges and solutions in the life sciences and environmental chemistry, Analytical and bioanalytical chemistry, 407 (2015) 6593-6617.
[22] D. Pozebon, G. Scheffler, V. Dressler, Recent applications of laser ablation inductively coupled plasma mass spectrometry (LA-ICP-MS) for biological sample analysis: a follow-up review, Journal of Analytical Atomic Spectrometry, 32 (2017) 890-919.
[23] D. Hare, B. Reedy, R. Grimm, S. Wilkins, I. Volitakis, J.L. George, R.A. Cherny, A.I. Bush, D.I. Finkelstein, P. Doble, Quantitative elemental bio-imaging of Mn, Fe, Cu and Zn in 6-hydroxydopamine induced Parkinsonism mouse models, Metallomics, 1 (2009) 53-58.
[24] B.P. Jackson, W.A. Hopkins, J. Baionno, Laser ablation-ICP-MS analysis of dissected tissue: a conservation-minded approach to assessing contaminant exposure, Environmental science & technology, 37 (2003) 2511-2515.
[25] J. Feldmann, A. Kindness, P. Ek, Laser ablation of soft tissue using a cryogenically cooled ablation cell, Journal of Analytical Atomic Spectrometry, 17 (2002) 813-818.
[26] D. Deiting, F. Börno, S. Hanning, M. Kreyenschmidt, T. Seidl, M. Otto, Investigation on the suitability of ablated carbon as an internal standard in laser ablation ICP-MS of polymers, Journal of Analytical Atomic Spectrometry, 31 (2016) 1605-1611.
[27] K. Zhang, D.S. Ivanov, R.A. Ganeev, G.S. Boltaev, P.S. Krishnendu, S.C. Singh, M.E. Garcia, I.N. Zavestovskaya, C. Guo, Pulse Duration and Wavelength Effects of Laser Ablation on the Oxidation, Hydrolysis, and Aging of Aluminum Nanoparticles in Water, Nanomaterials, 9 (2019) 767.
[28] D.A. Frick, D. Günther, Fundamental studies on the ablation behaviour of carbon in LA-ICP-MS with respect to the suitability as internal standard, Journal of Analytical Atomic Spectrometry, 27 (2012) 1294-1303.
[29] M. Resano, E. Garcia-Ruiz, F. Vanhaecke, Laser ablation–inductively coupled plasma–dynamic reaction cell–mass spectrometry for the multi-element analysis of polymers, Spectrochimica Acta Part B: Atomic Spectroscopy, 60 (2005) 1472-1481.
[30] J.-L. Todolí, J.-M. Mermet, Study of polymer ablation products obtained by ultraviolet laser ablation—inductively coupled plasma atomic emission spectrometry, Spectrochimica Acta Part B: Atomic Spectroscopy, 53 (1998) 1645-1656.
[31] D.A. Frick, C. Giesen, T. Hemmerle, B. Bodenmiller, D. Günther, An internal standardisation strategy for quantitative immunoassay tissue imaging using laser ablation inductively coupled plasma mass spectrometry, Journal of Analytical Atomic Spectrometry, 30 (2015) 254-259.

[32] M. Debeljak, J. van Elteren, K. Vogel-Mikuš, Development of a 2D LA-ICP-MS mapping procedure for mercury in maize (Zea mays L.) root cross-sections, Anal. Chim. Acta, 787 (2013) 155-162.
[33] T. Van Helden, S. Braeuer, T. Van Acker, O. Leroux, D. Van Der Straeten, F. Vanhaecke, High-speed mapping of Hg and Se in biological tissue via laser ablation-inductively coupled plasma-mass spectrometry, Journal of Analytical Atomic Spectrometry, (2022).
[34] H.A. Wang, D. Grolimund, C. Giesen, C.N. Borca, J.R. Shaw-Stewart, B. Bodenmiller, D. Günther, Fast chemical imaging at high spatial resolution by laser ablation inductively coupled plasma mass spectrometry, Analytical chemistry, 85 (2013) 10107-10116.
[35] S.J. Van Malderen, J.T. van Elteren, F. Vanhaecke, Development of a fast laser ablation-inductively coupled plasma-mass spectrometry cell for sub-µm scanning of layered materials, Journal of Analytical Atomic Spectrometry, 30 (2015) 119-125.
[36] S.J. Van Malderen, T. Van Acker, F. Vanhaecke, Sub-micrometer nanosecond LA-ICP-MS imaging at pixel acquisition rates above 250 Hz via a low-dispersion setup, Analytical chemistry, 92 (2020) 5756-5764.
[37] C. Neff, P. Becker, D. Günther, Parallel flow ablation cell for short signal duration in LA-ICP-TOFMS element imaging, Journal of Analytical Atomic Spectrometry, 37 (2022) 677-683.
[38] T. Van Acker, S.J. Van Malderen, T. Van Helden, C. Stremtan, M. Šala, J.T. van Elteren, F. Vanhaecke, Analytical figures of merit of a low-dispersion aerosol transport system for high-throughput LA-ICP-MS analysis, Journal of Analytical Atomic Spectrometry, 36 (2021) 1201-1209.
[39] S.J. Van Malderen, A.J. Managh, B.L. Sharp, F. Vanhaecke, Recent developments in the design of rapid response cells for laser ablation-inductively coupled plasma-mass spectrometry and their impact on bioimaging applications, Journal of Analytical Atomic Spectrometry, 31 (2016) 423-439.
[40] A. Jerše, K. Mervič, J.T. van Elteren, V.S. Šelih, M. Šala, Quantification anomalies in single pulse LA-ICP-MS analysis associated with laser fluence and beam size, Analyst, 147 (2022) 5293-5299.
[41] A. Schweikert, S. Theiner, M. Šala, P. Vician, W. Berger, B.K. Keppler, G. Koellensperger, Quantification in bioimaging by LA-ICPMS-Evaluation of isotope dilution and standard addition enabled by micro-droplets, Analytica Chimica Acta, 1223 (2022) 340200.
[42] M. Šala, V.S. Šelih, J.T. van Elteren, Gelatin gels as multi-element calibration standards in LA-ICP-MS bioimaging: fabrication of homogeneous standards and microhomogeneity testing, Analyst, 142 (2017) 3356-3359.
[43] T. Van Acker, S.J. Van Malderen, M. Van Heerden, J.E. McDuffie, F. Cuyckens, F. Vanhaecke, High-resolution laser ablation-inductively coupled plasma-mass spectrometry imaging of cisplatin-induced nephrotoxic side effects, Analytica chimica acta, 945 (2016) 23-30.
[44] R. Hafidz, C. Yaakob, I. Amin, A. Noorfaizan, Chemical and functional properties of bovine and porcine skin gelatin, International Food Research Journal, 18 (2011) 787-791.
[45] B.J. Wood, D.J. Smythe, T. Harrison, The condensation temperatures of the elements: A reappraisal, American Mineralogist: Journal of Earth and Planetary Materials, 104 (2019) 844-856.
[46] D.J. Kutscher, M.B. Fricker, B. Hattendorf, J. Bettmer, D. Günther, Systematic studies on the determination of Hg-labelled proteins using laser ablation-ICPMS and isotope dilution analysis, Analytical and bioanalytical chemistry, 401 (2011) 2691-2698.
[47] X. Guo, R.E. Sturgeon, Z. Mester, G.J. Gardner, Photochemical alkylation of inorganic arsenic Part 1. Identification of volatile arsenic species, Journal of Analytical Atomic Spectrometry, 20 (2005) 702-708.
[48] J. Feldmann, R. Grümping, A. Hirner, Determination of volatile metal and metalloid compounds in gases from domestic waste deposits with GC/ICP-MS, Fresenius' journal of analytical chemistry, 350 (1994) 228-234.
[49] F. Vanhaecke, R. Dams, C. Vandecasteele, 'Zone model'as an explanation for signal behaviour and non-spectral interferences in inductively coupled plasma mass spectrometry, Journal of Analytical Atomic Spectrometry, 8 (1993) 433-438.
[50] E. Sutcliffe, R. Srinivasan, Dynamics of UV laser ablation of organic polymer surfaces, Journal of applied physics, 60 (1986) 3315-3322.

[51] A. Vogel, V. Venugopalan, Mechanisms of pulsed laser ablation of biological tissues, Chemical reviews, 103 (2003) 577-644.